RSC Advances

ROYAL SOCIETY OF CHEMISTRY

www.rsc.org/advances

Graphene oxide-enwrapped Bi_2WO_6 composites as a highly efficient catalyst for the thermal decomposition of cyclotrimethylenetrinitramine

Yu Zhang[a,b], Libai Xiao[c], Kangzhen Xu[a,*], Jirong Song[a], Fengqi Zhao[c]

[a] *School of Chemical Engineering, Northwest University, Xi'an 710069, PR China*

[b] *College of Chemistry and Chemical Engineering, Xinyang normal University, Xinyang 464000, PR China*

[c] *Xi'an Modern Chemistry Research Institute, Xi'an 710065, PR China*

Abstract: A novel approach for the construct of graphene oxide (GO) enwrapped Bi_2WO_6 nanocomposites (GBWe) by modifying the surface charge of Bi_2WO_6 nanoparticles (NPs) has been described. The product showed a 3D interconnected network structure with little aggregation and increased high active surface area. The catalytic effect of GBWe on the thermal decomposition of cyclotrimethylenetrinitramine (RDX) was comparatively investigated with GO, Bi_2WO_6 NPs, GO and Bi_2WO_6 mixed by simply ultrasonic blend. The results indicated that GBWe exhibits the best catalytic activity. The exothermic peak was significantly decreased by 34.4 °C and the endothermic peak disappeared. Meanwhile, the apparent activation energy (E_a) was reduced by 65.6 kJ mol^{-1}. This enhanced catalytic effect should be attributed to the synergistic effect between GO and Bi_2WO_6 NPs.

Keywords: GO, Bi_2WO_6, En-wrapping, Catalytic activity, RDX, Thermal decomposition

1. Introdution

The combustion of solid propellant is a complicated transfer process of mass and energy. To a great extent, the burning rate depends on the contact area of oxidizers and combustibles as well as the effect of burning catalyst. Over the past few years, substantial efforts have been devoted to the development of a single metal oxide and two physically mixed components as combustion catalyst. The most commonly used catalysts are transition metal oxides, such as Fe_2O_3[1,2], CuO[3], Co_3O_4[3,4], Bi_2O_3[5] and NiO[6]. As demonstrated, binary mixed metal oxides have better catalytic effect than a single one, because the performance of two kinds of metal oxides would be

* Corresponding author.
E-mail address: xukz@nwu.edu.cn

mutually complementary and have a “synergistic effect”[7-9].

Cyclotrimethylenetrinitramine (RDX) is one of the most common oxidizers in the domain of composite solid propellants and gun propulsion because of their energetic and smokeless features, and its thermal decomposition performance has a great influence on the combustion behavior of propellants[10-13]. Numerous metal oxides have been evaluated for the thermal decomposition of RDX[14,15].

Metal composite oxide Bi_2WO_6, known as one of the simplest Aurivillius oxides with stable perovskite structure and good chemical stability[16-18], has received considerable attention in recent years due to its excellent intrinstic physical and chemical performances[17-20]. Recently, we designed Bi_2WO_6 nanoparticles (NPs) and controlled their morphology as well as size by adjusting the reaction parameters[21]. As shown in the further experiments, Bi_2WO_6 NPs exhibited the brilliant application in solid propellant, which not only greatly enhanced the burning rate and reduced the pressure exponent, but formed a specific high-pressure “plat-form” at 12~22 MPa. However, the NPs inevitably suffer from the problems of aggregation in practical applications owing to the relatively higher surface energy and smaller size. To circumvent these obstacles, the well dispersion of these NPs into a nanosheet surfaces is expected to have excellent conductive and catalytic properties. Therefore, the generation of GO-based functional materials have attracted substantial research efforts motivated by the desire to combine the properties of two functional nanoscale materials to achieve a wider range of applications such as catalyst[22,23], sensors[24], solar cells[25], supercapacitors[26] and lithium ion batteries[27,28].

Graphene oxide (GO), one of the most important derivatives of graphene, is an atomic-layer-thick material bearing oxygen functional groups on its basal planes and edges[29]. These oxygen-containing groups on GO can be used to operate their self-assembly with other components via different non-covalent forces[30-32]. On the other hand, as 2D nanosheets with superb mechanical flexibility and large surface area, GO sheets are appropriate candidates for en-wrapping NPs[33,34]. By this means, GO sheets can coat the surface of NPs, and then significantly hinder the aggregation of NPs. Additionally, the thin conductive GO sheets are beneficial for the application of

the NPs in catalysts. To control the en-wrapping process, the critical issue is to solve the incompatibility between GO and NPs.

Herein, we reported a simple, efficient and environmentally benign strategy for obtaining GO sheets-enwrapped Bi_2WO_6 nanocomposites. Firstly, Bi_2WO_6 was modified to render positive charge by tuning the surface pH value which benefits from its insolubility in acid-base chemistry, then the positively charged Bi_2WO_6 nanoparticles were assembled with negatively charged GO by the mutual electrostatic interactions. This material, which was defined as GBWe, showed a uniform three-dimensional (3D) interconnected structure, suppressed the aggregation of NPs, and resulted in closely integrated interface and high surface area. Compared with free Bi_2WO_6 NPs, GO and simply mixing GO and Bi_2WO_6 NPs, the resulting GBWe nanocomposites exhibit higher catalytic activity on the decomposition of RDX.

Fig. 1 Schematic illustrating the fabrication processes of GO-enwrapped Bi_2WO_6 nanocomposites (GBWe)

2. Experimental

2.1. Synthesis of Bi_2WO_6

The Bi_2WO_6 NPs were prepared by hydrothermal method as reported by our group[21], which are detailed as below. 2 mmol $Na_2WO_4 \cdot 2H_2O$ was dissolved into 40 mL ethylene glycol under stirring, following which 1.0 g PVP was added as

dispersants, and then 4 mmol $Bi(NO_3)_3 \cdot 5H_2O$ was put into the homogenous solution. After that, the pH of mixture was adjusted to 10.0 using NaOH solution, stirring and yielding a stable white suspension. The resulting mixture was sealed in a 50 mL Teflon-lined stainless-steel autoclave and maintained at 160 ºC in air for 20 h. Finally, the obtained precipitates were collected through centrifugation, washed with ethanol and deionized water several times and dried at 60 ºC.

2.2. Synthesis of GBWe

GO was prepared according to a modified Hummers method[35] and exfoliated in distilled water with a concentration of 1 mg mL^{-1} for later use. 0.27 g as-prepared Bi_2WO_6 NPs were dispersed in water by ultrasonic method for 30 min, and then 0.1 mol L^{-1} HCl was introduced to get modified Bi_2WO_6 NPs by adjusting the pH to 5. After that, 30 mL prepared GO aqueous solution was added and the mixture was treated by ultrasonic for another 2 h. Finally, the resulting GBWe was filtered, washed and dried. The detailed synthesis is schematically illustrated in Fig. 1. For comparison, a hybrid called GBWu was prepared by mixing GO with Bi_2WO_6 NPs via simply ultrasonic blending without tuning the pH value.

2.3. Characterization

X-ray diffraction (XRD) patterns were acquired using a Rigarku Mini Flex 600 X-ray diffractometer with Cu Kα radiation. Raman spectroscopy was carried out using an INVIA Raman microprobe (Renishaw Instruments) with a 532 nm laser source and a 50 × objective lens. X-ray photoelectron spectroscopy (XPS) measurements were performed using a Thermo Scientific ESCALAB 250Xi X-ray photoelectron spectrometer. Scanning electron microscopy (SEM) images were recorded using a Zeiss SIGMA scanning electron microscope. Transmission electron microscopy (TEM) images and high-resolution TEM (HR-TEM) images were obtained using an FEI Tecnai G2 microscope operated at 200 kV.

2.4. Catalytic measurements

The catalytic effect of GBWe composite on the thermal decomposition of RDX was investigated by differential scanning calorimetry (DSC). At first, GBWe was mixed with RDX at a mass ratio of 1:4 respectively, and grounded gently in the agate mortar

to the good uniformity. Then the resulting mixture was detected using a 200F3 differential scanning calorimeter (Netzsch, Germany) for DSC with the following conditions: nitrogen gas purity, 99.999%; N_2 flow rate, 40 mL min^{-1}; sample mass, approximately 0.5 mg; heating rate (β), 2.5, 5.0, 7.5 and 10.0 °C min^{-1}.

The catalytic performance of GO, Bi_2WO_6 NPs and GBWu were also carried out in the same way as comparison.

3. Results and discussion

The crystalline structure of the samples were identified by XRD, and the typical wide-angle diffraction patterns are shown in Fig. 2. The diffraction pattern of GO has a peak centered at around 2θ = 12.5 °, corresponding to the (001) interplanar spacing of 0.71 nm. For the XRD patterns of Bi_2WO_6, the seven well-defined diffraction peaks can be indexed to an orthorhombic Bi_2WO_6 crystalline structure (JCPDS 39-0256). In GBWu composite, a (001) reflection peak of GO can be observed. The weak intensity is due to the less content of GO in the composite. Nevertheless, no diffraction peak of GO appears on the XRD pattern of GBWe, indicating that the regular stacks of GO have been destroyed and exfoliated during the self-assembly process between GO and Bi_2WO_6.

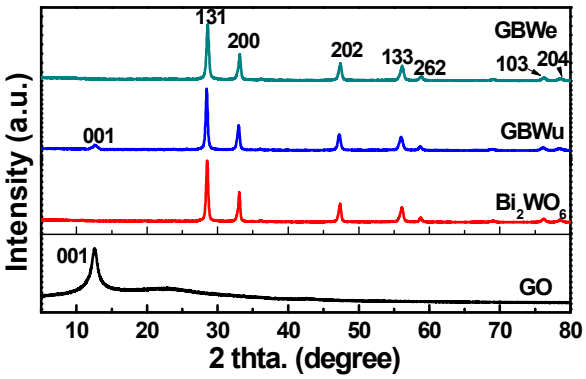

Fig. 2. XRD patterns of GO, Bi_2WO_6, GBWu and GBWe

Raman spectra of GO and as-prepared samples are illustrated in Fig. 3. Two characteristic peaks of GO are located at around 1335 and 1586 cm^{-1}, corrseponding to the D and G bands, respectively. Here, the G band attributes to the scattering of the E_{2g} mode of sp^2 carbon atoms, while the D band reflects intervalley scattering[33,34]. The structure of pure Bi_2WO_6 is orthorhombic with $P2_1ab$ space group, which is able

to be considerably derived from parent phase of I4/mmm symmetry[36]. For the Raman spectrum of pure Bi_2WO_6, the bonds of 793 and 825 cm^{-1} can be respectively assigned to the symmetric (A_{1g}) and antisymmetric (A_{2u}) stretching modes of WO_6 groups which involve the motions of apical oxygen atoms[36]. The weak peak at 705 cm^{-1} is associated with the asymmetric (E_u) stretching mode of WO_6 octahedra that mainly involves the vibrations of equatorial oxygen atoms. The bonds in the 180~600 cm^{-1} can be attributed to the bending modes of WO_6 octahedra coupled with the stretching and bending modes of Bi-O polyhedra[37]. The bending modes of WO_6 octahedra consist of 224 (E_u), 261 (E_u), 282 (E_g), 303 (E_g) and 416 (E_u) cm^{-1}. The bending mode of Bi-O polyhedra is at 333 (B_{1g}) cm^{-1}[37]. The peaks at 143 and 151 cm^{-1} may be specified as the translations of tungsten and bismuth ions[38]. GBWe and GBWu show typical Raman peaks of the D and G bonds. Moreover, the D and G bonds of GBWe exhibit no significant changes in comparison with these of GO, suggesting that GO was not reduced under the applied conditions and existed as a component of GBWe. However, Raman spectra of GBWe and GBWu show the symmetric stretching A_{1g} modes of WO_6 groups at 800 cm^{-1}, the bending E_g modes of WO_6 octahedras at 303 cm^{-1}, and lattice modes of bismuth ions at 152 cm^{-1}, which are shifted to higher energy in comparision with pure Bi_2WO_6. The shift and broadening in the Raman peaks could be caused by GO residing in the complexes.

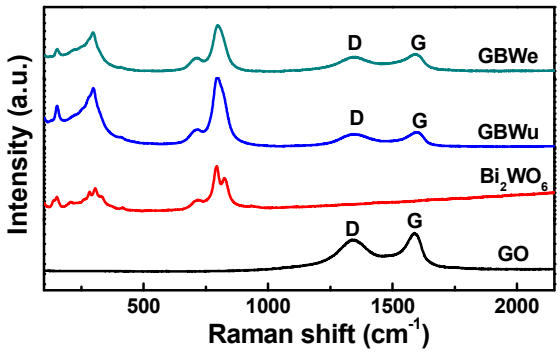

Fig. 3. Raman spectra of GO, Bi_2WO_6, GBWu and GBWe

XPS was further carried out to determine the chemical compositions and bonding character. The high resolution spectra of W 4f and Bi 4f in GBWe are displayed in Fig. 4a,b. For the spectrum of W 4f (Fig. 4a), the peaks at 35.3 and 37.4 eV could be

assigned to W 4f $_{7/2}$ and W 4f $_{5/2}$ for the W^{+6} oxidation state[39]. As shown in Fig. 4b, the XPS spectrum of Bi 4f can be fitted by two peaks at 158.9 and 164.3 eV, corresponding to Bi 4f $_{7/2}$ and Bi 4f $_{5/2}$ spin-orbit of Bi^{3+} species[39].

Fig. 4c, c', c" present the C 1s XPS spectra of GBWe, GO and Bi_2WO_6 NPs, respectively. In the case of GO (Fig. 4c'), three types of carbons with different chemical states are observed at 284.9, 287.1 and 288.2 eV, which are corresponded to neutral (C–C bond with sp^2 orbital), ether (C–O) and carboxyl (C=O) carbons, respectively [33]. The C1s XPS spectrum of pure Bi_2WO_6 (Fig. 4c") also shows three peaks at 284.7 (C–C bond with sp^2 orbital), 286.4 (C–O), and 288.0 (C=O) eV[40]. After the en-wrapping process (Fig. 4c), the peak positions of C–C (sp^2), C–O and C=O groups in GBWe are located at 286.1 eV, 287.8 eV and 289.5 eV, respectively, which shift toward higher binding energies, implying the interaction between GO sheets and Bi_2WO_6 is a simple electrostatic interactions but also an electron transfer between GO sheets and Bi_2WO_6.

The O 1s XPS spectra of GBWe, GO and Bi_2WO_6 NPs are shown in Fig. 4d, d', d". For GO (Fig. 4d'), deconvolution of the O 1s spectrum generates four peaks at 531.4, 532.5, 533.2, and 534.1 eV, which are attributed to C=O, C–O, C–O–C and oxygen from adsorbed water groups, respectively[32,33]. The O1s XPS spectrum of pure Bi_2WO_6 (Fig. 4d") can only be deconvoluted into three peaks at 529.8 eV (oxygen in the crystal lattice of Bi_2WO_6), 531.0 eV (hydroxyl species) and 532.9 eV (oxygen from adsorbed water groups)[41]. Alternatively, the O1s spectrum of GBWe can be fitted by four peaks (Fig. 4d). The 529.7 eV peak should belong to the crystal lattice oxygen in pure Bi_2WO_6. The peaks at 530.9 and 532.8eV provide a further evidence for the existence of oxygen groups on GO surface in the form of C=O and C–O. And the peak at 534.0 eV can be assigned to oxygen from adsorbed water groups. The result of XPS analysis reveals the coexistence of GO and Bi_2WO_6 in GBWe.

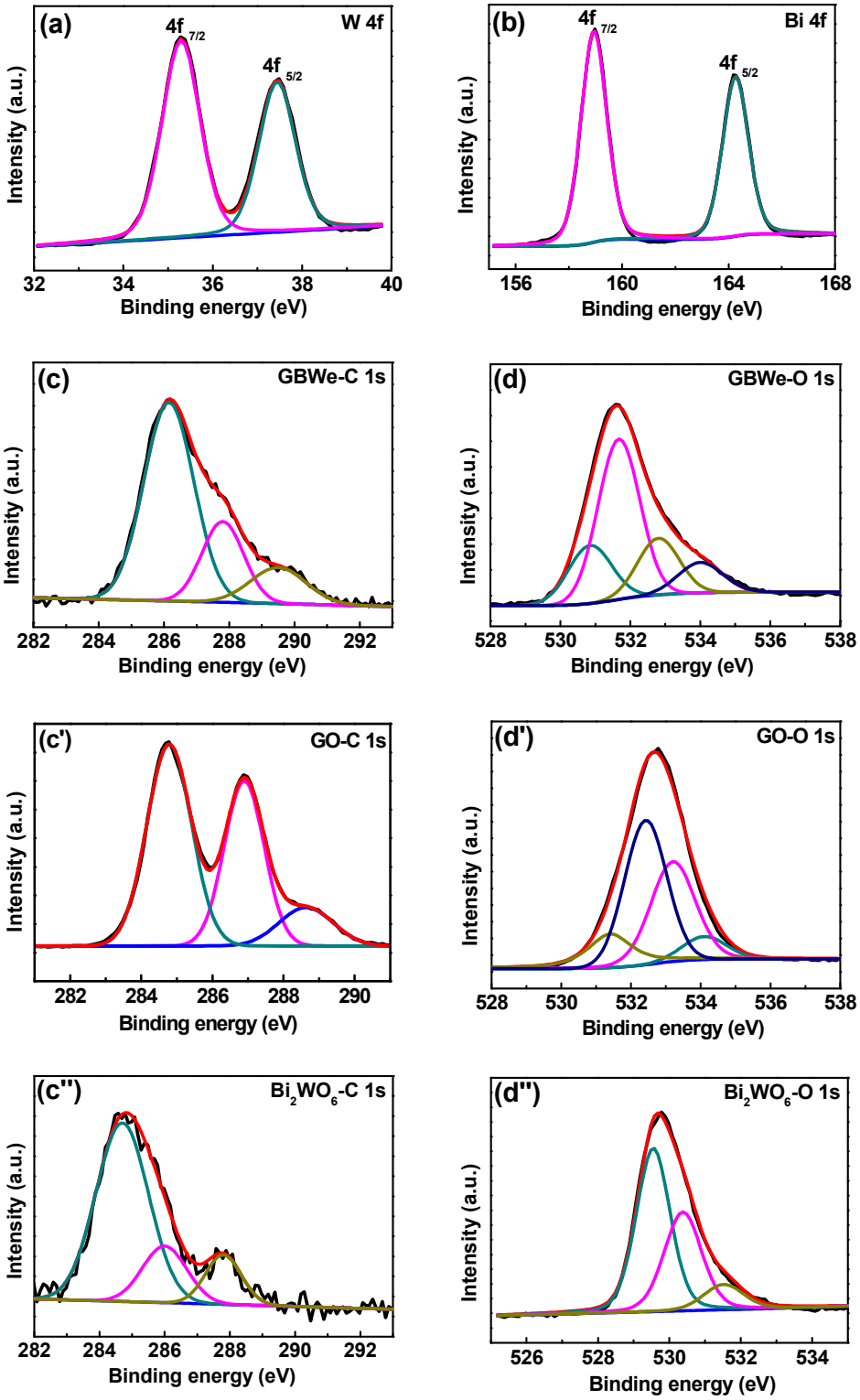

Fig. 4. XPS characterization: (a) W 4f and (b) Bi 4f spectra of GBWe;

C 1s spectra of (c) GBWe, (c') GO and (c") Bi_2WO_6;

O 1s spectra of (d) GBWe, (d') GO and (d") Bi_2WO_6.

The morphology and physical structure of Bi_2WO_6 NPs and GBWe nanocomposite were elucidated by SEM and TEM measurements, which are presented in Fig. 5. In Fig. 5a, the as-prepared Bi_2WO_6 NPs have a well-define spherical structure and close-packed arrays with diameters of about 40 nm. As shown in the image of GBWu (Fig 5b), a very few Bi_2WO_6 NPs are scattering in GO thin sheets, the majority remain the agglomerate state. What's more, GO sheets are not completely exfoliated, but show little effect on decreasing the aggregation of Bi_2WO_6 NPs. From Fig. 5c, it can be observed that Bi_2WO_6 NPs exist homogeneously in the whole GO single sheet without obvious aggregation. The high-magnification SEM image (Fig. 5d) is clearly presented that the GO sheets are tightly en-wrapped on the surface of Bi_2WO_6 NPs and appear transparent with wrinkled and rough textures. In TEM image (Fig. 5e), we are still able to catch sight of a 3D interconnected network GO en-wrapped Bi_2WO_6 NPs structure. Significantly, the formation of GBWe is associated with good mechanical flexibility and relatively large lateral size of GO sheets, which will not only help to greatly prohibit the aggregation and increase the high active surface area of Bi_2WO_6 NPs, but also enhance the diffusion rate of reaction molecules and electrons. Simultaneously, the H^+ modified Bi_2WO_6 NPs can be considered to play an important role to prevent the re-stacking of GO sheets. In order to verify the crystalline structure of GBWe, we showed the HRTEM image (Fig. 5f). The thin GO sheets can be easily distinguished from the Bi_2WO_6 NPs by their fringe parts. Bi_2WO_6 NPs show a clear lattice plane with perfect crystallinity, and the lattice fringe with interplanar spacing of 0.312 nm corresponds to the (131) plane, in agreement with the XRD analysis. All the test results suggest unambiguously that GO sheets have successfully en-wrapped Bi_2WO_6 NPs.

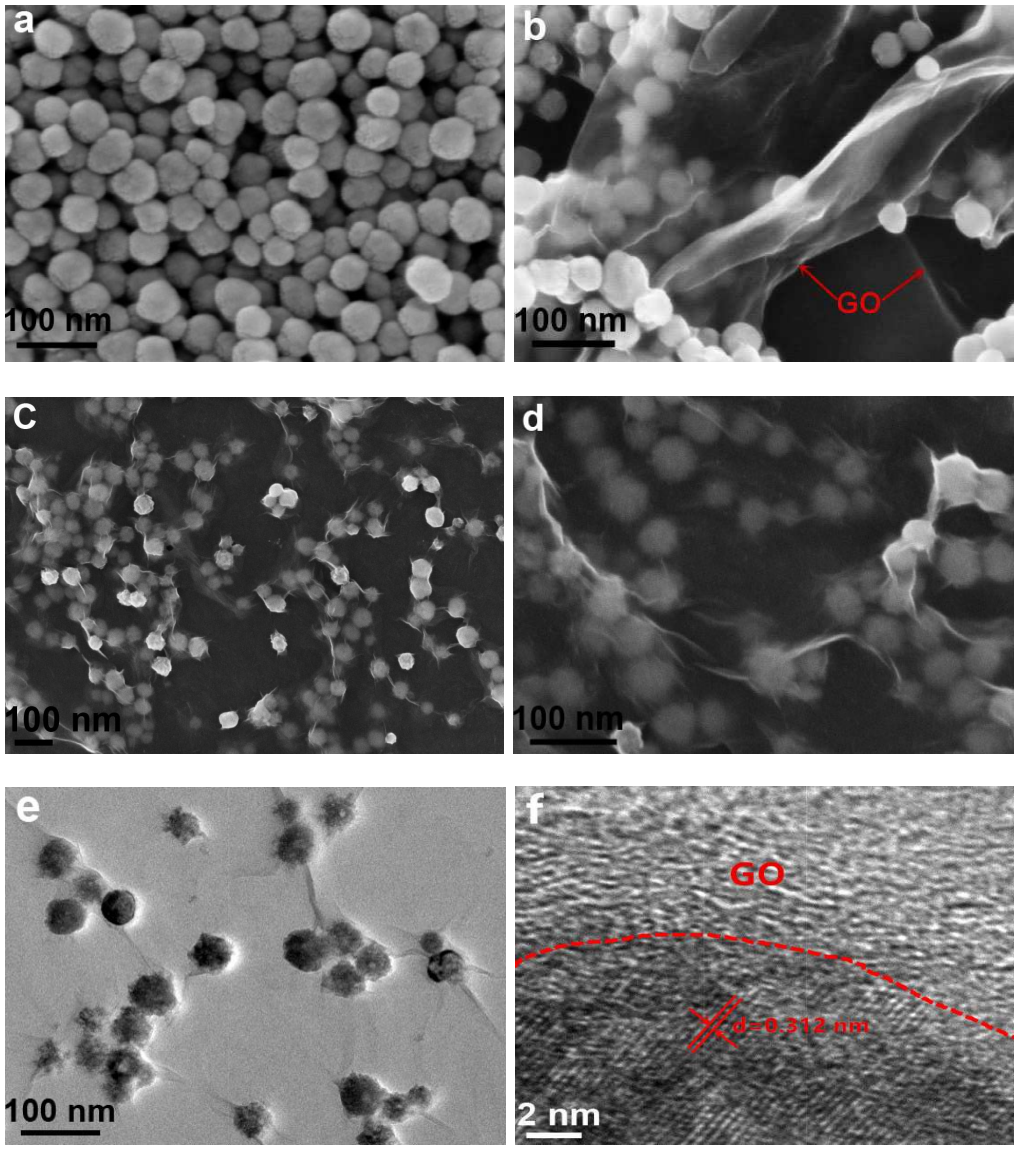

Fig. 5. SEM images of (a) Bi_2WO_6 and (b) GBWu;

low (c) high (d) magnfication SEM images of GBWe;

(e) TEM image of GBWe; (f) HRTEM image of GBWe.

The thermal decomposition of RDX dramatically influence the properties of solid propellants: the lower thermal decomposition temperature and apparent activation energy, the shorter ignition delay time, the higher burning rate of propellant[3,9]. The catalytic activities of GO, Bi_2WO_6 NPs, GBWu and GBWe for the thermal decomposition of RDX were determined by DSC method with a heating rate of 10 ℃ min^{-1}, and the results were presented in Fig. 6. As shown in DSC curves of pure RDX, the thermal decomposition process consists of two stages. In the first stage, a sharp

endothermic peak appears at 205°C could be assigned to the melting of RDX. In the subsequent stage, the exothermic reaction takes place, leading to the strong peak at 242.9 °C, which is ascribed to the complete decomposition of RDX[14,42]. The apparent decomposition heat of pure RDX is 797 J g^{-1}. When Bi_2WO_6 NPs are added, the exothermic peak is merely shifted down by 1.7 °C and the corresponding decomposition heat is increased to 853 J g^{-1}. Adding GO allows the change of the exothermic peak from 242.9 to 225.8 °C; moreover, the heat is also rose to 978 J g^{-1}. In the presence of GBWu, the exothermic peak occurs at 225.4 °C with the heat of 983 J g^{-1}. While mixing RDX with GBWe, we find that the endothermic peak disappears, there is a sole exothermic peak at 208.5 °C, which is decreased by 34.4 °C. Meanwhile, the decomposition heat is 1816 J g^{-1}, increased greatly by 1019 J g^{-1}.

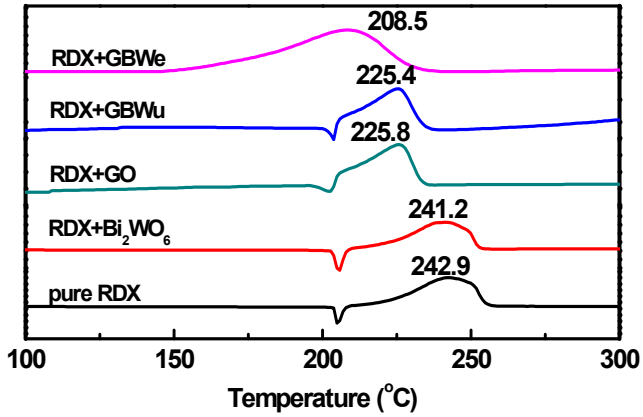

Fig. 6. DSC curves of pure RDX and RDX mixed with different samples

To further measure the catalytic performance of the four samples, the apparent activation energy value (E_a) of the decomposition process can be calculated by the following relationship in the equation (1) between exothermic peak temperature and temperature and heating rate (2.5, 5.0, 7.5, 10 °C min^{-1}).

$$\ln\frac{\beta}{T_p^{\,2}} = \ln\frac{AR}{E_a^{\,2}} - \frac{E_a}{RT_p} \qquad (1)$$

where β is the heating rate in degrees Celsius per minute, T_p is the peak temperature, R is the ideal gas constant, and A is the pre-exponential factor. According to equation (1), the activation energy (E_a) can be obtained from the slope of the line resulting from the plot of $\ln(\beta/T_p^{\,2})$ as a function of $1/T_p$. The results are summarized in Table 1.

The E_a of pure RDX is approximately 172.6 kJ mol^{-1} in the reports[9,43]. In the

presence of GBWe, we can see that E_a of RDX decomposition is dramatically decreased to 107.0 kJ mol^{-1}. While Bi_2WO_6 NPs, GO and GBWu as additives lower the activation energy to 126.4, 122.0 and 115.9 kJ mol^{-1} , respectively.

Table 1 Apparent activation energies of RDX decomposition in the presence of different catalysts

Sample	β^a (°C min^{-1})	$T_p{}^b$ (°C)	E_a (kJ mol^{-1})	r^c
RDX+Bi_2WO_6	2.5	219.2	126.4	0.998
	5	229.4		
	7.5	235.2		
	10	241.2		
RDX+GO	2.5	204.6	122.0	0.982
	5	213.2		
	7.5	217.5		
	10	225.8		
RDX+GBWu	2.5	203.4	115.9	0.988
	5	211.5		
	7.5	218.6		
	10	225.4		
RDX+GBWe	2.5	186.8	107.0	0.984
	5	194.1		
	7.5	202.6		
	10	208.5		

[a] Heating rate. [b]The exothermic peak temperature. [c]The linear correlation coefficient.

From the above results, it can be concluded that GO shows higher catalytic effect on the decomposition of RDX in comparison with Bi_2WO_6 NPs. In theory, Bi_2WO_6 NPs possess many active sites that can exhibit a high catalytic performance on the decomposition of RDX, however, the aggregation would tremendously weaken their catalytic capability[44]. As for GO, owing to its thin conductive sheets, the decomposition molecules and electrons in GO move much faster than they do among Bi_2WO_6 NPs, which yields a better catalytic activity. Remarkably, the catalytic properties of GBWe is superior to both the individual component (GO and Bi_2WO_6 NPs) and ultrasonic hybrid (GBWu). It has been well addressed that electrons in GO move a lot faster than they do among metal oxide atoms[45]. The formation of GO-enwrapped Bi_2WO_6 NPs could form an excellent charge transfer pathways and offer accelerated electrons to speed up the decomposition processes. Moreover, GO

possesses large theoretical surface area of 2600 m^2 g^{-1}[34], which can effectively inhibit the aggregation and increase the exposed active sites of Bi_2WO_6 NPs, accelerating the catalysis process. Accordingly, the catalytic effect of GBWe is strongly enhanced by the synergistic effect between GO and Bi_2WO_6 NPs. Furthermore, hybrid GBWu is not as effective as the en-wrapped composites GBWe. It is speculated that GO sheets could not be completely exfoliated and uniformly dispersed with Bi_2WO_6 NPs with the absence of electrostatic interaction. Consequently, the electrostatic interactions between the H^+ modified Bi_2WO_6 nanoparticles and negatively charged GO play a key role in the synergistic catalytic effect on the thermal decomposition of RDX.

4. Conclusion

In conclusion, we have reported a simple, efficient and environmentally benign approach to fabricate GO sheets-enwrapped Bi_2WO_6 nanocomposites (GBWe). In this procedure, the self-assembly GO and Bi_2WO_6 NPs were driven by electrostatic forces, which benefits from the introduced H^+. SEM and TEM observations illustrate that Bi_2WO_6 NPs exist homogeneously in the whole GO single sheet with little aggregation, leading to a remarkable catalytic performance on the thermal decomposition of RDX. The presence of GBWe significantly lowers the decomposition temperature by 34.4 °C and decreases the apparent activation energy (E_a) by 65.6 kJ mol^{-1} compared with pure RDX. Due to the synergistic effect between GO and Bi_2WO_6 NPs, GBWe shows better catalytic action than the individual components (GO and Bi_2WO_6 NPs) and ultrasonic hybrid (GBWu). Therefore, GBWe can be a hopeful candidate for solid propellants, which may initiate new opportunities in the field of high-energy propellants.

Acknowledgments

This investigation received financial assistance from the National Natural Science Foundation of China (21241003), Postdoctoral Science Foundation of China (2014M552480) and Postdoctoral Science Foundation of Shaanxi Province.

References

1 Y. Yuan, J. Wei, Y. J. Wang, P. Shen, F. S. Li, P. Y. Li, F. Q. Zhao and H. X. Gao, *Appl. Surf. Sci.*, 2014, **303**, 354-359.

2 S. Shioya, M. Kohga and T. Naya, *Combust. Flame*, 2014, **161**, 620-630.

3 E. Alizadeh-Gheshlaghi, B. Shaabani, A. Khodayari, Y. Azizian-Kalandaragh and R. Rahimi, *Powder Technol.*, 2012, **217**, 330-339.

4 L. N. Jin, Q. Liu and W. Y. Sun, *CrystEngComm.*, 2012, **14**, 7721-7726.

5 W. L. Hong, F. Q. Zhao, J. H. Liu, D. Y. Tian, Z. K. Luo and L. H. Diao, *Chin. J. Explosives& Propellants.,* 2003, **26**, 37-39.

6 J. K. Sharma, P. Srivastava, G. Singh, G. Singh, M. S. Akhtar and S. Ameen, *Cream. Int.*, 2015, **41,** 1573-1578.

7 Y. P. Wang, X. J. Yang, L. D. Lu and X. Wang, *Thermochimica Acta*., 2006, **443**, 225-230.

8 X. D. Zheng, P. Li, S. L. Zheng and Y. Zhang, *Powder Technol*., 2014, **268**, 446-451.

9 Y. Zhang, T. T. Wei, K. Z. Xu, Z. Y. Ren, L. B. Xiao, J. R. Song and F. Q. Zhao, *RSC Adv.*, 2015, **5**, 75630-75635.

10 H. W. Qiu, V. Stepanov, A. R. D. Stasio, T. G. Chou and W. Y. Lee, *J. Hazard. Mater.*, 2011, **185**, 489-493.

11 C. Wang, M. E. Fuller, C. Schaefer, J. L. Caplan and Y. Jin, *J. Hazard. Mater.*, 2012, **217-218**, 187-193.

12 T. Naya and M. Kohga, *Aerosp. Sci. Technol.*, 2014, **32**, 26-34.

13 Q. Q. Qiu, K. Z. Xu, S. H. Yang, Z. Gao, H. Zhang, J. R. Song and F. Q. Zhao, *J. Solid State Chem.*, 2013, **205**, 205-210.

14 Z. X. Wei, L. Wei, L. Gong, Y. Wang and C. W. Hu, *J. Hazard. Mater.*, 2010, **177**, 554-559.

15 H. Ren, Y. Y. Liu, Q. J. Jiao, X. F. Fu and T. T. Yang, *J. Phys. Chem. Solids.*, 2010, **71**, 149-152.

16 D. K. Ma, S. M. Huang, W. X. Chen, S. W. Hu, F. F. Shi and K. L. Fan, *J. Phys. Chem. C.*, 2009, **113**, 4369-4374.

17 F. Amano, A. Yamakata, K. Nogami, M. Osawa and B. Ohtani, *J. Am. Chem. Soc.*, 2008, **130**, 17650-17651.

18 Z. J. Zhang, W. Z. Wang, J. Xu, M. Shang, J. Ren and S. M. Sun, *Catal. Commun.*, 2011, **13**, 31-34.

19 Y. L. Tian, B. B. Chang, J. L. Lu, J. Fu, F. N. Xi and X. P. Dong, *ACS Appl. Mater. Inter.*, 2013, **5**, 7079-7085.

20 J. Y. Sheng, X. J. Li and Y. M. Xu, *ACS Catal.*, 2014, **4**, 732-737.

21 T. T. Wei, Y. Zhang, K. Z. Xu, Z. Y. Ren, H. X. Gao and F. Q. Zhao, *RSC Adv.*, 2015, **5,** 70323-70328.

22 N. Li, Z. F. Geng, M. H. Cao, L. Ren, X. Y. Zhao, B. Liu, Y. Tian and X. W. Hu, *Carbon*, 2013, **54**, 124-132.

23 J. C. Liu, H. W. Bai, Y. J. Wang, Z. Y. Liu, X. W. Zhang and D. D. Sun, *Adv. Funct. Mater.*, 2010, **20**, 4175-4181.

24 R. K. Joshi, P. Carbone, F. C. Wang, V. G. Kravets, Y. Su, I. V. Grigorieva, H. A. Wu, A. K. Giem and R. R. Nair, *Science*, *2014,* **343**, 752-754.

25 C. Ge, H. J. Li, M. J. Li, C. P. Li, X. G. Wu and B. H. Yang, *Carbon*, 2015, **95**, 1-9.

26 W. L. Meng, X. Zhou, Z. L. Qiu, C. W. Liu, J. W. Chen, W. J. Yue, M. T. Wang and H. Bi, *Carbon*, 2016, **96**, 532-540.

27 S. Chen, J. W. Zhu, X. D. Wu, Q. F. Han and X. Wang, *ACS Nano.*, 2010, **2**, 2822-1830.

28 H. L. Wang, Y. Yang, Y. Y. Liang, J. T. Robinson, Y. G. Li, A. Jackson, Y. Cui, and H. J. Dai *Nano Lett*., 2011, **11**, 2644-2647.

29 S. B. Yang, X. L. Feng, S. Ivanovici and K. Mullen, *Angew. Chem. Int. Ed.*,. 2010, **49**, 8408 -8411.

30 O. C. Compton, Z. An, K. W. Putz, B. J. Hong, B. G. Hauser, L. C. Brinson and S. T. Nguyen, *Carbon*, 2012, **50**, 3399-3406.

31 Q. Liu, J. B. Shi, M. T. Cheng, G. L. Li, D. Cao and G. B. Jiang, *Chem. Commun*., 2012, **48**, 1874-1876.

32 R. Thiruvengadathan, S.W. Chung, S. Basuray, B. Balasubramanian, C.S. Staley, K. Gangopadhyay and S. Gangopadhyay, *Langmuir*, 2014, **30**, 6556-6564.

33 J. Zhao, Z. S. Liu, Y. L. Qin and W. B. Hu, *CrystEngComm*., 2014, **16**, 2001-2008.

34 D. Q. Wu, F. Zhang, H. W. Liang and X. L. Feng, *Chem. Soc. Rev.*, 2012, **41**, 6160-6177.

35 W. S. Hummers and R. E. Offeman. *J. Am. Chem. Soc.*, 1958, **80**, 1339-1339.

36 M. Maczka, L. Macalik, K. Hermanowicz, L. Kepinski and P. Tomaszewski, *J. Raman Spestrosc.*, 2010, **41**, 1059-1066.

37 H. C. Gupta, Archana and V. Luthra, *J. Mol. Struct.*, 2011, **1005**, 53-58.

38 M. Hojamberdiev, K. Katsumata, K. Morita, S. A. Bilmes, N. Matsushita and K. Okada, *Appl.*

Catal. A-Gen., 2013, **457**, 12-20.

39 Y. Tian, L. D. Zhang and J. X. Zhang, *J. Alloy. Compound.*, 2012, **537**, 24-28.

40 M. Blanco, P. Alvarez, C. Blanco, M. V. Jimenez, J. Fernandez-Tornos, J. J. Perez-Torrente, J. Blasco, G. Subías, V. Cuartero, L. A. Oro, R. Menéndez, *Carbon.*, 2016, **96**, 66-74.

41 S. Sriwichai, H. Ranwongsa, K. Wetchakun, S. Phanichphant and N. Wetchakun, *Superlattice. Microst.*, 2014, **76**, 362-375.

42 G. Hussain and G. J. Rees, *Fuel.*, 1995, **74**, 273-277.

43 X. P. Fan, X. Wang, Z. R. Liu and H. M. Tan, *Energ. Mater.*, 2005, **13**, 284-287.

44 J. W. Zhu, G. Y. Zeng, F. D. Nie, X. M. Xu, S. Chen, Q. F. Han and X. Wang, *Nanoscale*, 2010, **2**, 988-994.

45 A. K. Geim, K.S. Novoselov , *Nat. Mater.*, 2007, **6**, 183-91.

GO sheets-enwrapped Bi_2WO_6 nanocomposites was obtained by a simple strategy and showed remarkable catalysis on the thermal decomposition of RDX.